



Submerged arc welding process: enhancement of production performance based on metallurgical observations

Romina Conte¹ · Francesco Raffaele Battista¹ · Giuseppina Ambrogio¹

Received: 7 May 2024 / Accepted: 15 July 2024 / Published online: 26 July 2024
© The Author(s) 2024

Abstract

Welding processes are widely used technologies in the industrial context for creating permanent connections between mechanical components. This popularity is due to their versatility, which arises from the numerous available process variants and the multiple advantages they offer compared to other joining techniques. In the manufacturing context, where devices often operate in extreme conditions, the quality of welds becomes a critical factor in ensuring the safety and reliability of the manufactured products. Furthermore, a sound joint requires careful compliance with the increasingly stringent design specifications demanded by customers who require industry-standard conformity in order to achieve defect-free, robust, and durable welds. To address these needs and to define the optimal roadmap for the investigated process condition, an experimental investigation was conducted on the submerged arc welding process. The experimental trials involved butt joints of ASTM A516 Gr.70 carbon steel plates with different thicknesses in a flat position, utilizing a U-shaped chamfer and a multi-pass welding technique. For each weldment, the effects of the main process parameters on the qualitative characteristics of the manufactured products were evaluated from a metallurgical perspective. This evaluation included an in-depth metallographic analysis of the heat-affected zone of the carbon steel joint and involved both the measurement of the dimensions of these areas as well as the amount of ferrite and pearlite that resulted as the phases observed in the final microstructure of the steel joint following its solidification. Furthermore, the joint quality was assessed with regard to mechanical strength through hardness measurements. By analysing the experimental data, the paper provides a valuable contribution for increasing the productivity of the investigated welding process, while simultaneously meeting the specified industrial quality requirements for the products made of medium-thickness carbon steels.

Keywords Joining · Arc welding · SAW · Multi-pass joint · Process optimization · Metallographic investigation

1 Introduction

Welding processes play a fundamental role in the manufacturing industry, significantly contributing to the fabrication of a wide range of products across diverse sectors. These sectors include automotive, aerospace, construction, shipbuilding, consumer goods, industrial machinery, infrastructure, and various applications, spanning from small-scale components to large structures [1, 2].

Welding is a primary technique for permanently join materials by applying an appropriate amount of energy. Its primary objective is to create strong and durable connections

between metal parts, often achieving a continuity of material at the microstructural level. This capability enables the fabrication of assemblies that require structural integrity. Furthermore, welded structures can be engineered to withstand different environmental conditions, making them suitable for use in a variety of settings [3, 4]. This adaptability is particularly crucial in industries where products are exposed to fluctuating temperatures, pressures and corrosive elements [5].

Ongoing research and innovation in welding techniques contribute to the development of new materials and processes. This innovation propels advancements in manufacturing technologies, resulting in improved product quality and performance. While welding is primarily used for connecting metallic materials, the numerous process variations also allow for the welding of polymeric, ceramic and composite materials [6–12].

✉ Romina Conte
romina.conte@unical.it

¹ University of Calabria, via Pietro Bucci, 45C, Rende, CS 87036, Italy

This study specifically focuses on a particular arc welding variant, namely the submerged arc welding process (SAW) [8]. SAW is commonly employed for joining large-sized components and thick material sections, particularly in industries such as shipbuilding, oil and gas and structural fabrication. It finds application in various contexts, including the construction of tube and pipeline joints, pressure vessels, nuclear containers, wind tower structures and the fabrication of oil, water or liquefied natural gas tanks [13–15]. SAW offers several key advantages, including (i) the high deposition rate and productivity; (ii) deep penetration, made possible by the high current intensities that can be utilized; (iii) the capability to weld thick and large pieces in a single pass and (iv) the ability to achieve high-quality welds [16, 17].

To perform the SAW process, it is essential to establish an arc between a continuously fed electrode (a wire) and the workpiece. The arc's parameters must be set to reach the melting temperature of both the base material and the filler material, allowing the creation of the weld bead. Temperature control plays a fundamental role in the joint formation, as a thermal cycle occurs during the welding process. This cycle induces changes in the metallurgical structure, affecting the material's microstructure and altering its physical and mechanical properties in the final joint [13].

The uniqueness of SAW lies in submerging the arc beneath a layer of granular flux, stored in a hopper. This granular flux acts as a protective coating over the molten pool, shielding it from the surrounding atmosphere. Moreover, it aids in reducing splatter and fumes, ultimately improving working conditions compared to other arc welding variants. It is important that the flux has a lower melting temperature and density than the base metal. During the process, a portion of the flux melts and solidifies over the weld bead, while the remaining granular flux is removed through an aspiration system at the end of each pass and then can be reused. The operation of the electric motor is controlled by a unit that ensures a continuous delivery of the wire from the coil through feeding rolls. This controlled wire speed ensures that the electrode wire's feed rate matches its melting rate, resulting in a stable and controlled arc [16, 17]. The operating principle of the SAW is depicted in Fig. 1.

Due to the inherent nature of the welding process, the materials involved are subjected to thermal cycles. A high specific heat input results in elevated temperatures and reduced cooling rates, which in turn promote the growth of crystalline grains. The cooling rate is also influenced by the thickness of the plates. In this context, thermal energy is primarily dissipated through conduction across the thickness of the two welded pieces, while the portion dissipated to the external environment through radiation and convection is negligible. The power losses to the external environment are further reduced due to the insulating behaviour of the granular flux which shields the molten

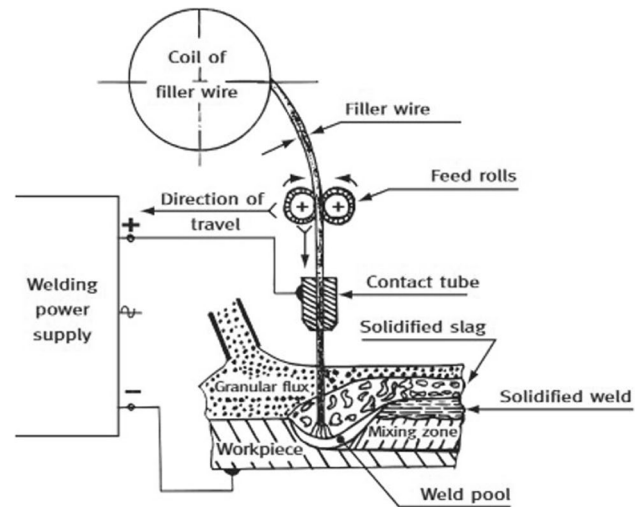


Fig. 1 Operating principle of the SAW [8]

pool during the welding process. Therefore, for the same specific heat input, the greater the thickness of the joint components, the faster their cooling occurs, leading to a more severe thermal cycle.

In this study, the focus was on a specific joint configuration, and on the analysis of the heat, dissipation within the material at the microscopic level was conducted. This analysis involved observing the heat-affected zone (HAZ), which represents the portion of the base material adjacent to the melted zone undergoing solid-state transformations. These transformations cause microstructural variations compared to the original base material. The grain morphology and the extent of the HAZ primarily depend on the base material used, especially regarding its chemical composition and its initial metallurgical structure, which is influenced by the manufacturing process adopted for sheet metal production, and on the welding process conditions. These latter determine the thermal cycle of the material; in fact, the main parameters which play a crucial role in these terms are the welding current, the arc voltage and the travel speed. Predicting the evolution of the microstructure within the HAZ can be challenging, especially in the case of multi-pass welding, as subsequent passes generate heating effects on the underlying microstructure obtained from previous passes [18].

Saleem and Lakshmanaswamy [19] focused on optimizing input setting parameters to enhance weld bead characteristics. They developed a mathematical model, and their experimental results closely matched the predicted values. Küçüköner et al. [20] used SAW to join two types of steel and assessed the quality and mechanical properties of the welded samples. Microstructure examinations revealed dendritic formation in the welded metal, with larger grains near the melting boundary on the primary material side.

Renwick [21] evaluated flux composition and its impact on the weld bead. Sharma and Chhibber [13] designed various submerged arc welding flux compositions using an extreme vertices design approach and studied their effects on the weld bead and mechanical properties. The flux, in combination with welding parameters, significantly influences arc stability and the final joint. Datta et al. [22] developed mathematical models to understand the influence of process parameters on the final geometry of the weld bead. Prasad and Dwivedi [23] investigated the effect on the microstructure and on the heat-affected zone. Rathi [24] highlighted that electrode diameter, trolley speed and wire feed rate are key factors for controlling weld bead dimensions. Vishwakarma and Dwivedi [25] applied the Taguchi method to optimize five welding parameters to achieve minimal hardness and maximum tensile strength.

The literature review underscores that the dimensions of the weld bead and all mechanical properties of the welded joint are significantly affected by several parameters of the welding process investigated. Understanding how to control the process is crucial for ensuring the mechanical performance of the welding joint and meeting quality standards required by the normative of the industrial sector considered as well as by the customers.

In this study, starting from an industrial benchmark configuration, a novel approach was investigated. Tests were performed by setting different combinations of process parameters, taking into account the voltage and current ranges imposed by the machine and the fixed travel speed values, but keeping constant the heat input, in order to optimize the process productivity and to preserve, at the same time, the mechanical properties of the specific joint configuration.

2 Materials and methods

2.1 Materials

ASTM A516 steel, also known as ASME SA516, was employed for the experimental tests of this work. It is a carbon-manganese steel, representing the standard specification for the fabrication of pressure vessels [26]. This material is typically chosen for applications with moderate to low operating temperatures due to its excellent notch toughness properties [27].

The ASTM A516 steel plates used in the experiments were obtained through the hot-rolling process. Specifically, the dimensions of the plates involved in the experimental tests were 100 mm in width, 400 mm in length and thicknesses of 10 mm and 25 mm.

ASTM A516 steel comes in different grades (55, 60, 65, and 70), each offering varying levels of mechanical

Table 1 Main mechanical properties of ASTM A516 Grade 70

Mechanical properties	Value
Ultimate tensile strength	510–650 MPa
Yield tensile strength	335 MPa
Elongation at break in 200 mm (min)	17%
Elongation at break in 50 mm (min)	21%

Table 2 Chemical composition of the base material (ASTM A516 Gr.70)

Component	Carbon, C	Manganese, Mn	Phosphorus, P	Silicon, Si	Sulfur, S
Weight percentage (%)	0.31	1.2	0.035	0.45	0.035

strength. Grade 70 is the one used to the aim of this work. It has higher yield strength and tensile strength values than other grades, providing higher tensile strength at low temperatures. These characteristics make it suitable for products operating under high-pressure conditions. Key mechanical properties of the material are summarized in Table 1.

Table 2 shows the chemical composition of the weld material. The main alloying elements in ASTM A516 Gr. 70 steel are carbon (*C*), manganese (*Mn*) and silicon (*Si*). The amount of these elements affects the mechanical properties of the material and its microstructure in a different manner. Indeed, *C* enhances heat treatment hardening and wear resistance in steels, but if it is present in excess, it results in the formation of martensite or bainite. These are undesirable structural constituents because they can lead to hydrogen cracking. *Mn* makes possible to increase the steel's toughness and contrasts the damaging effects of sulfur, but it causes a deterioration of the material's resilience property. In addition, from the microstructural point of view, it was found that the presence of *Mn* (1.37 wt. %) in ASTM A516 Gr. 70 steel promoted the acicular ferrite formation in the joint molten zone and reduced the grain size of polygonal ferrite in heat-affected regions in multi-pass welds [27]. Finally, the presence of *Si* increases the strength and hardenability of steels and acts as a deoxidizer; however, it negatively affects the toughness and weldability of the material.

In addition to the mentioned elements, ASTM A516 carbon steel also contains other alloying elements, including molybdenum, chromium, and nickel, albeit in smaller quantities. These elements enhance the hardenability of the material, with nickel contributing to increased toughness. It is worth noting that an excess of molybdenum can lead to the formation of phases that can reduce notch toughness at low temperatures.

Table 3 Chemical composition of AWS 5.17 EH 14

Component	Carbon, C	Manganese, Mn	Phosphorus, P	Silicon, Si	Sulfur, S	Copper, Cu
Weight percentage (%)	0.10	1.8	0.019	0.05	0.013	0.05

Table 4 Main mechanical properties of AWS 5.17 EH14

Mechanical properties	Value
Ultimate tensile strength	550 MPa
Yield tensile strength	470 MPa
Elongation at break in 200 mm (min)	30%

As for the filler material for the welded joint, a low-carbon steel coded as AWS 5.17 of EH14 grade was used.

This high-Mn, copper-coated solid wire is typically employed in single-pass and multi-pass SAW procedures.

The chemical composition of the electrode used is provided in Table 3 while Table 4 lists its key mechanical properties.

The filler wire was selected to achieve a chemical composition and mechanical strength of the joint metal similar to that of the base material. Two different filler wire diameters, specifically 2.5 mm and 4 mm, were used during welding tests, based on the pass type.

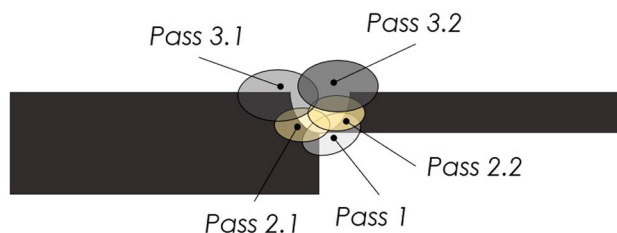
Finally, the covering flux used for the experiments was the ESAB OK 10.61, a highly basic agglomerated flux commonly used for SAW. Its nominal density is 1.1 kg/dm³ and nominal basicity index is 2.6.

2.2 Methods

As mentioned previously, the SAW process is a widely utilized electric arc welding method in heavy industries for joining medium and thick metals. It relies on an electric current passing between the filler wire and the workpiece to generate the thermal energy needed for material melting. Due to its operational characteristics and the equipment involved, the SAW can only be conducted in fully automatic or semi-automatic mode. In this study, the semi-automatic mode was employed.

Tests were conducted using the LINCOLN ELECTRIC's Place Power Wave® AC/DC 1000 SD CE machine, designed and suitable only for SAW. The machine carries an output rating of 1000 Amps and 44 Volts at 100% duty cycle.

The plates were butt-welded in a flat position, and a total of five passes were performed. Figure 2 illustrates the procedure used for creating the joints. The test execution method involved initially coupling plates of varying thicknesses to create the first root weld pass (referred to as pass 1 in Fig. 2) at room temperature. A 2.5-mm-diameter electrode was used for this purpose, providing support for the plates during the subsequent weld bead formation.

**Fig. 2** Schematization of the numbering of the passes sequence during the experimental tests

A milling operation was then conducted on the opposite side of the previously welded area to create a groove, as indicated in Fig. 2. This groove was then filled by performing four additional passes along the milled channel, using a 4-mm diameter filler wire. It is important to note that no plate preheating or post-weld heat treatment was performed. The process parameters set for each pass are the arc voltage (V), the welding current (I) and the travel speed (v). The selected values for these parameters are provided in the next paragraph. It is worth highlighting that the machine ranges (specifically the maximum values) in terms of current and voltage have been considered, while the travel speed could be set only considering preset values (i.e. 320, 384, 448, 512, 544, 576, 608, 672, 704, 768 mm/min).

These parameters play a crucial role in the welding process and determines the amount of heat input introduced in the workpiece. Higher current values result in increased arc intensity and penetration depth, leading to a larger resistant section of the joint under external loads. The travel speed, on the other hand, is inversely proportional to the thermal input which the material is exposed to. Both too low and too high travel speeds can result in significant defects within the weld bead.

The influence of current, voltage and travel speed on the weld bead and on the microstructure has been assessed. To this aim, the transformation phases that occur usually in steels during welding process have been analysed. These phases depend on the specific heat input, which is a key process variable encompassing all three individual investigated parameters [16], as well as on the cooling rate of the workpiece. The specific heat input is calculated using the following equation:

$$Q[J/mm] = \frac{\eta * V * I * 60}{ws} \quad (1)$$

where η represents the arc efficiency factor, and in case of the SAW, it is equal approximately to 0.95 [28], V , I and w_s are, as already specified, the arc voltage, the welding current and the welding speed, respectively.

The dimensions of the molten and the heat-affected zone, as well as of their grain size, depend on the amount of heat (Q) transferred to the material during the welding. Besides, the transient thermal cycle plays a crucial role in controlling the material's cooling rate, which, in turn, is a key factor in determining phase changes and the formation of microstructural constituents.

3 Experimental investigation

3.1 The experimental plan

For the experimental analysis, specific working conditions were established. As previously mentioned, a constant number of passes for each sample was considered, and it was set at five owing to the depth of the welding gap. Table 5 outlines the designed experimental plan and the values assigned to voltage, current and welding speed. It is essential to note that test 0 represents the working condition necessary to achieve a sound joint in accordance with UNI EN ISO 3834

quality standards; therefore, it was considered as a benchmark. Consequently, the experimental plan was constructed by maintaining a constant specific heat input for each pass, based on test 0. The first pass was consistent across all tests, as it was performed on the bottom side of the plates to create a foundational layer that supports subsequent welding steps. The second passes (labelled pass 2.1 and pass 2.2) had varying parameters in each test, but the nominal specific heat input for all of them was approximately 2145 J/mm. The third passes (labelled pass 3.1 and pass 3.2) were conducted by employing the same process parameters in all tests, aligning with the specific heat input of test 0, which was approximately 1790 J/mm.

3.2 The experimental procedure

As mentioned, the experimental investigation aimed to assess how process parameters affect joint quality and process efficiency by reducing the time required for welding. To evaluate the process accuracy, a metallurgical analysis of the final joints was conducted, focusing on the thermal effects caused by the process parameters. Specifically, the HAZ, the microstructure and the mechanical properties of the joints have been examined and discussed below.

Table 5 Standard condition and experimental plan

No. of test	No. of pass	Voltage (V)	Electrical current (A)	Welding speed (mm/min)	Nominal specific heat input (J/mm)
Test 0 (benchmark)	1	27	440	320	2227.50
	2.1	26	440	320	2145.00
	2.2	26	440	320	2145.00
	3.1	29.5	550	544	1789.52
	3.2	29.5	550	544	1789.52
Test 1	2.1	34	404	384	2146.25
	2.2	34	404	384	2146.25
Test 2	2.1	25.4	540	384	2143.13
	2.2	25.4	540	384	2143.13
Test 3	2.1	34	471	448	2144.73
	2.2	34	471	448	2144.73
Test 4	2.1	32	500	448	2142.86
	2.2	32	500	448	2142.86
Test 5	2.1	29.7	540	448	2147.95
	2.2	29.7	540	448	2147.95
Test 6	2.1	34	539	512	2147.58
	2.2	34	539	512	2147.58
Test 7	2.1	32	573	512	2148.75
	2.2	32	573	512	2148.75
Test 8	2.1	34	605	576	2142.71
	2.2	34	605	576	2142.71
Tests 1–8	3.1	34	675	768	1792.97
	3.2	34	675	768	1792.97

It should be pointed out that geometric effects and the resulting induced potential stresses were disregarded in the following discussion since they were assumed unchanged in the several tests. Indeed, it was possible to assume identical distortions for all the tests due to the method of performing the experimental trials. In fact, in each test the sequence and number of weld passes remained unchanged as well as the mechanical constraint conditions, interpass temperatures and the overall heat input value for each welding pass.

3.2.1 Sample preparation

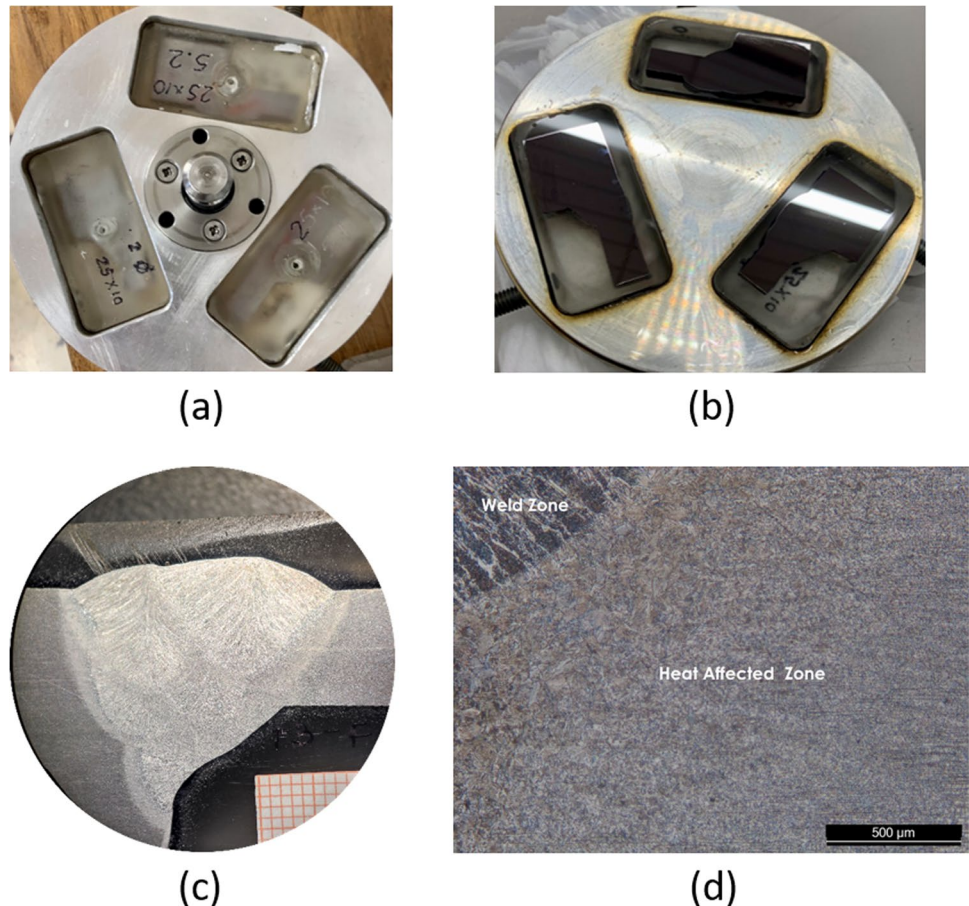
To conduct the required studies, samples have been extracted from the joined plates by cutting them at low temperatures. This was done to avoid the alteration of the microstructure already affected by the welding process. From each weld bead, three samples have been extracted to ensure result repeatability and account for the non-uniformity of the weld bead along the entire joined plates.

Before conducting macro and micro analysis, all specimens underwent a specific preparation process to eliminate cutting-induced scratches. First, the samples were

cold-mounted using acrylic resin to prevent thermal alterations. The drying time for this process was approximately 45 min. Once the samples were ready, they were secured in the holder of the Struers Tegramin-25 machine (as shown in Fig. 3a), and their surfaces were prepared for metallographic inspection. The preparation involved the use of abrasive papers with different granularities to remove residual resin and achieve a flat surface. Subsequently, specific cloths were used for mirror polishing (Fig. 3b). The samples were prepared by chemically treating their polished surfaces with a 3% nitric acid-based solution, named Nital, for 25 s. This treatment made the macrostructure of the weld beads clearly visible to the naked eye (Fig. 3c), allowing each pass to be distinctly recognized, as well as under the microscope (Fig. 3d).

It is important to note that the immersion time in the solution was determined through experimental observations. Several tests were conducted to establish the right immersion time required to reveal the joint microstructure. Low time (underetching) was insufficient for visualizing the grains, while prolonged immersion (overetching) resulted in a surface burning effect from a microstructure perspective.

Fig. 3 a Mounted samples, b polished samples, c macrograph of the weld bead, d micrograph of the HAZ



3.2.2 Metallurgical observations

Metallographic investigations were conducted using the LEICA DM 4000M microscope. The applied method, as outlined in Fig. 4, enabled the analysis of the heat-affected zone (HAZ). For this purpose, at least three pictures were captured close to each welding pass to provide a comprehensive description of the entire joint microstructure.

To determine the amount of microstructural constituents at room temperature, specifically ferrite and pearlite, micrographs were analysed using a specific image processing technique that allowed distinguishing and estimating the magnitudes of those two components.

The micrograph displayed in Fig. 4b shows the distinction between *base material* (not affected by heat) and *region 1* and *region 2*, which belong to the HAZ and are characterized by differences in microstructure, morphology and grain size. More in detail, *region 1* refers to the part of the HAZ bordering the base material, while *region 2* indicates the area adjacent to the weld bead.

3.2.3 Hardness measurement

Vickers microhardness measurements were performed in order to assess the mechanical strength of the welds obtained. The mechanical characterization of the weldments was executed using the Micro Combi Tester hardness

machine (CSM Instruments SA, Switzerland) on mounted, polished and chemically etched specimens. The test load was increased linearly to a maximum value of 3 N at a loading rate of 6 N/min for a time of 15 s. Microhardness measurements were performed focusing on welding passes 2.1, which, as described later, are of great interest in assessing the effects of different process parameters on welded joint quality. Figure 5 provides a schematic pattern of the indentation grid for the microhardness measurement relative to welding pass 2.1 of test specimen T8. Specifically, indentations were performed along four lines orthogonal to the weld bead running through pass 2.1 in order to assess hardness values in the welded zone, in the HAZ regions (i.e. *region 1* and *region 2*), as well as in the base material. For this purpose, a 50-micron distance was set between two consecutive measurements.

4 Discussion of the results

The welded joints were observed through an optical microscope in order to investigate their microstructure and welding-induced phase transformations. Since the welding passes were performed with the same heat input value for passes 2.1 and 2.2 in which the process parameters were changed, the thermal cycle experienced by the material was the same for each test. This resulted in a similar microstructure for each

Fig. 4 Metallographic investigation of the welded joints: **a** identification of the HAZ produced by pass 2.1, **b** micrograph at 5x of the HAZ

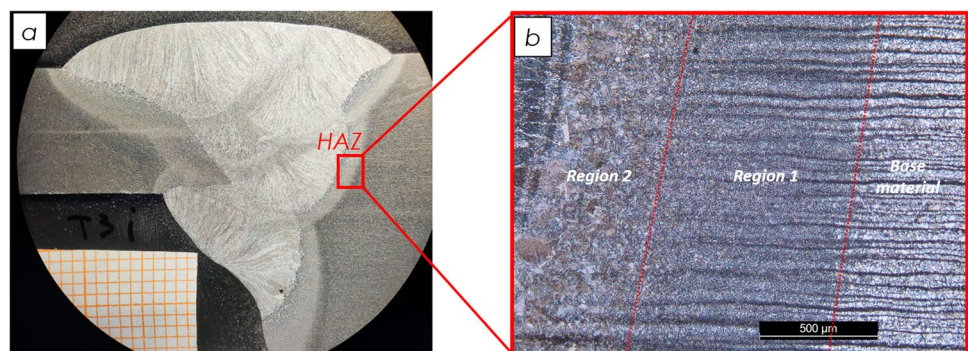
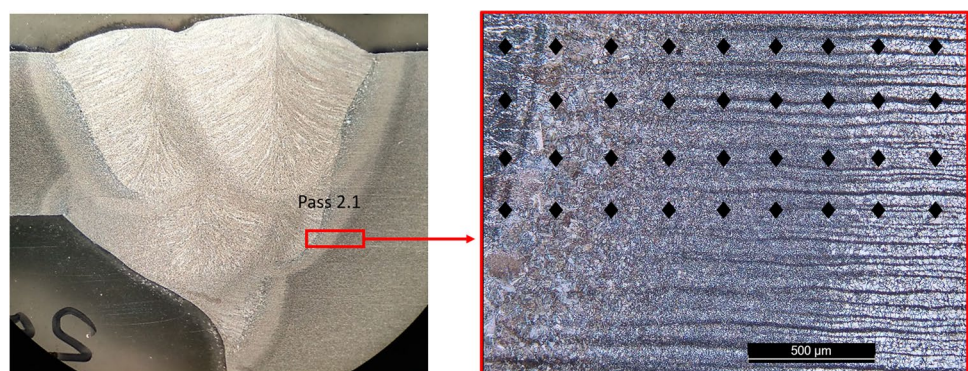


Fig. 5 Representation of the indentation grid for hardness measurement of welded joints for pass 2.1 relative to T8 specimen



test specimen. Figure 6 shows the distinctive microstructures of the base material (a), HAZ *region 1* (b), and HAZ *region 2* (c), at 50x magnification, respectively.

The base material is a hypoeutectoid C-Mn steel (according to ASTM A516 Gr. 70 specifications) with a carbon content of 0.31% by weight. Its microstructure (Fig. 6a) is composed of coarse ferrite grains with an equiaxial morphology, i.e. approximately the same dimension in all directions, and thin pearlite bands aligned in the rolling direction. The average ferritic grain area in the base material is approximately $183 \mu\text{m}^2$. This value was obtained as the average of several measurements taken using an image processing software on micrographs with 50x magnification.

Region 1 of the HAZ is the region of the parent material that reached such a temperature during welding that resulted in recrystallization, i.e. a grain refinement. Indeed, the microstructure in *region 1* presents equiaxial ferrite grains with a considerably lower average size than those in the base material (Fig. 6b). Specifically, the average grain area in *region 1* is approximately $41 \mu\text{m}^2$. Furthermore, the pearlite bands were clearly distorted.

Region 2 of the HAZ reached a higher maximum temperature during the welding thermal cycle and therefore experienced different phase transformations, as well as a slower cooling rate than *region 1*. This resulted in a different microstructure in both grain size and morphology (Fig. 6c). Specifically, the distinctive microstructure of *region 2* consists of pro-eutectoid ferrite and Widmanstätten ferrite. Following the complete austenitization of the grains at high temperatures, pro-eutectoid ferrite with a polygonal shape initially formed from the austenitic grain boundaries during the cooling of the steel. Phase transformation from austenite to pro-eutectoid ferrite occurred until the eutectoid temperature was reached. Below this temperature, a second phase transformation occurred, i.e. the austenite that was not transformed into ferrite is transformed into ferrite plates separated by thin cementite regions starting from the austenite grain boundaries. This grain morphology is referred to as Widmanstätten ferrite.

Since *region 2* of the HAZ reached a higher maximum temperature and was characterized by a lower cooling rate than *region 1*, grain growth occurred in this area. As can be observed from the comparison of Fig. 6b, c, the grain size is significantly larger in *region 2* even though the grain morphology is different. Due to the evidence of this phenomenon and the significant difference between the microstructures of *regions 1* and *2*, a grain size comparison between these two HAZ regions was not feasible.

Being ferrite very low in carbon content, its high level within the investigated region can mainly be explained by two physical phenomena occurring during the steel welding. The first one is the decarbonisation, i.e. the loss of C from the base material due to its reaction with the oxygen in the air, while the second one is related to the migration of C atoms from a higher to a lower content area. In fact, the material of the HAZ is the ASTM A516 Gr.70 steel, and it has a C content of 0.31% by weight, which is higher than that in the melted zone. Indeed, the latter is a mixture of base and filler metal, with a carbon content of about 0.10%, as already specified in Table 3.

To examine the effects of the different working parameters on the microstructural characteristics of welded plates, the focus of the study was placed on the HAZ. Both regions constituting the HAZ were analysed in order to estimate the ferrite content, which could be representative of the weakest portion of the joint.

An image processing software was employed to this aim. Micrographs at 50x magnification (Fig. 7a–c) were converted into black-and-white images (Fig. 7b–d). Ferrite was clearly identified because of the white colouring, while the pearlite was dark. Therefore, the percentage of ferrite was determined by calculating the ratio of white pixels to the total ones. It is important to note that the method of calculating these values relates to ferrite as a phase, thus, to the amount of ferrite in both the pro-eutectoid and Widmanstätten ferrite structural constituent.

Quantitative analyses were conducted to determine the average extension of the overall HAZ and the size of *regions*

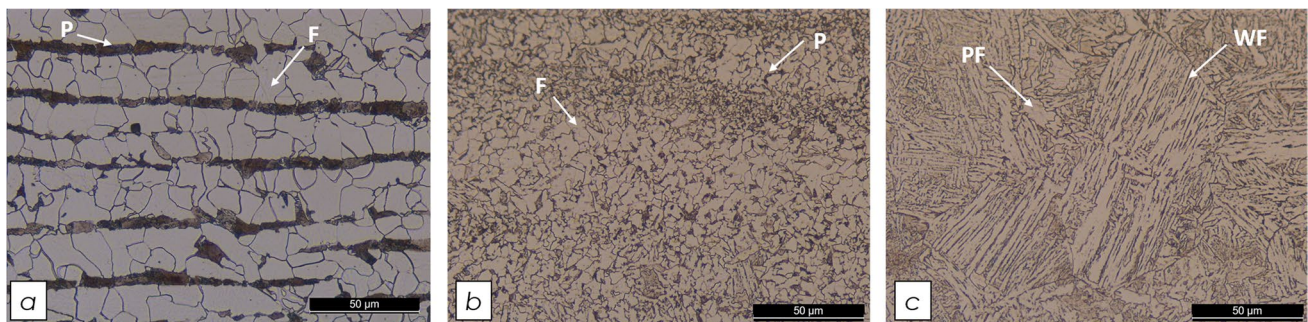
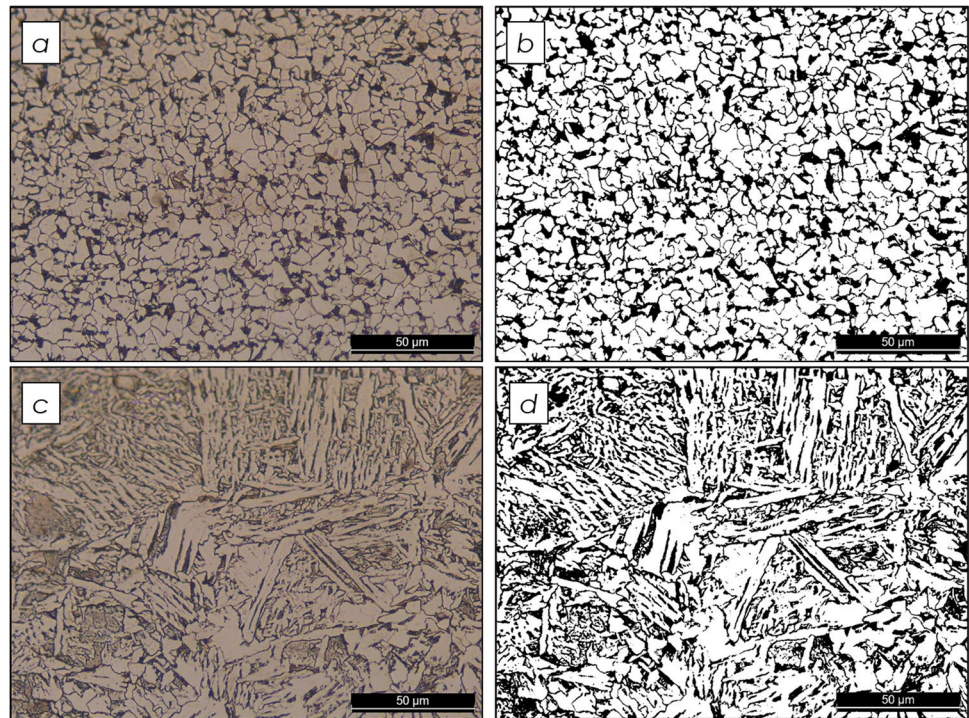


Fig. 6 Microstructure of the **a** base material, **b** HAZ *region 1*, and **c** HAZ *region 2* at 50x magnification. P pearlite, F ferrite, PF pro-eutectoid ferrite, WF Widmanstätten ferrite

Fig. 7 **a** *Region 1* micrograph at 50x and **b** its ferritic (69%) and pearlitic (31%) content; **c** *region 2* micrograph at 50x and **d** its ferritic (75%) and pearlitic content (25%)



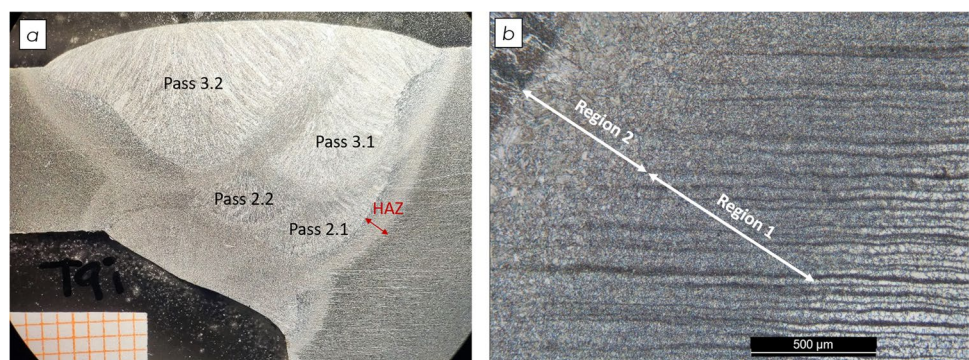
1 and 2 for each welding pass. In Fig. 8a, for instance, pass 2.1 is indicated by a red arrow, denoting the length of the entire HAZ produced at the end of the process, whereas Fig. 8b shows a 5x magnification micrograph of the HAZ produced by pass 2.1 for the same specimen. On this latter, the white arrows indicate the extension of *region 1* and *region 2* resulting from the welding. To determine the lengths of both the HAZ and the two regions, multiple equally spaced lengths were measured, considering potential variations along the edge of each welding pass. For each pass, the lengths were obtained by means of segments orthogonal to the weld boundary line. Ten length measurements were taken for each welding pass to ensure consistency and repeatability of results.

Additionally, the percentage of ferrite within *region 1* and *region 2* was estimated following the above-mentioned

procedure. Data collected from the regions under investigation were then analysed by comparing the different working conditions set in the experimental study (Table 5). First of all, the data related to *pass 2.1* were considered, since, looking for instance at Fig. 8a, *pass 2.2* was covered by *pass 3.1* and *pass 3.2* making an assessment of the corresponding outputs impossible. Just for test 2, test 5 and test 7, it was possible to compare the effect caused by pass 2.2, as it was not covered by subsequent pass 3.

Histograms in Fig. 9a display the extension of the HAZ produced by *pass 2.1* for each considered test, while Fig. 9b reports the extension of *region 2*. From the histogram observation, it is easy to deduce that *region 1* area is wider than that of the *region 2*. Figure 9c and d show, respectively, the percentage of ferrite within *region 1* and *region 2*.

Fig. 8 **a** Example of an analysed macrograph and indication of the passes and of the HAZ extension, **b** 5x micrograph and indication of *region 1* and *region 2* length



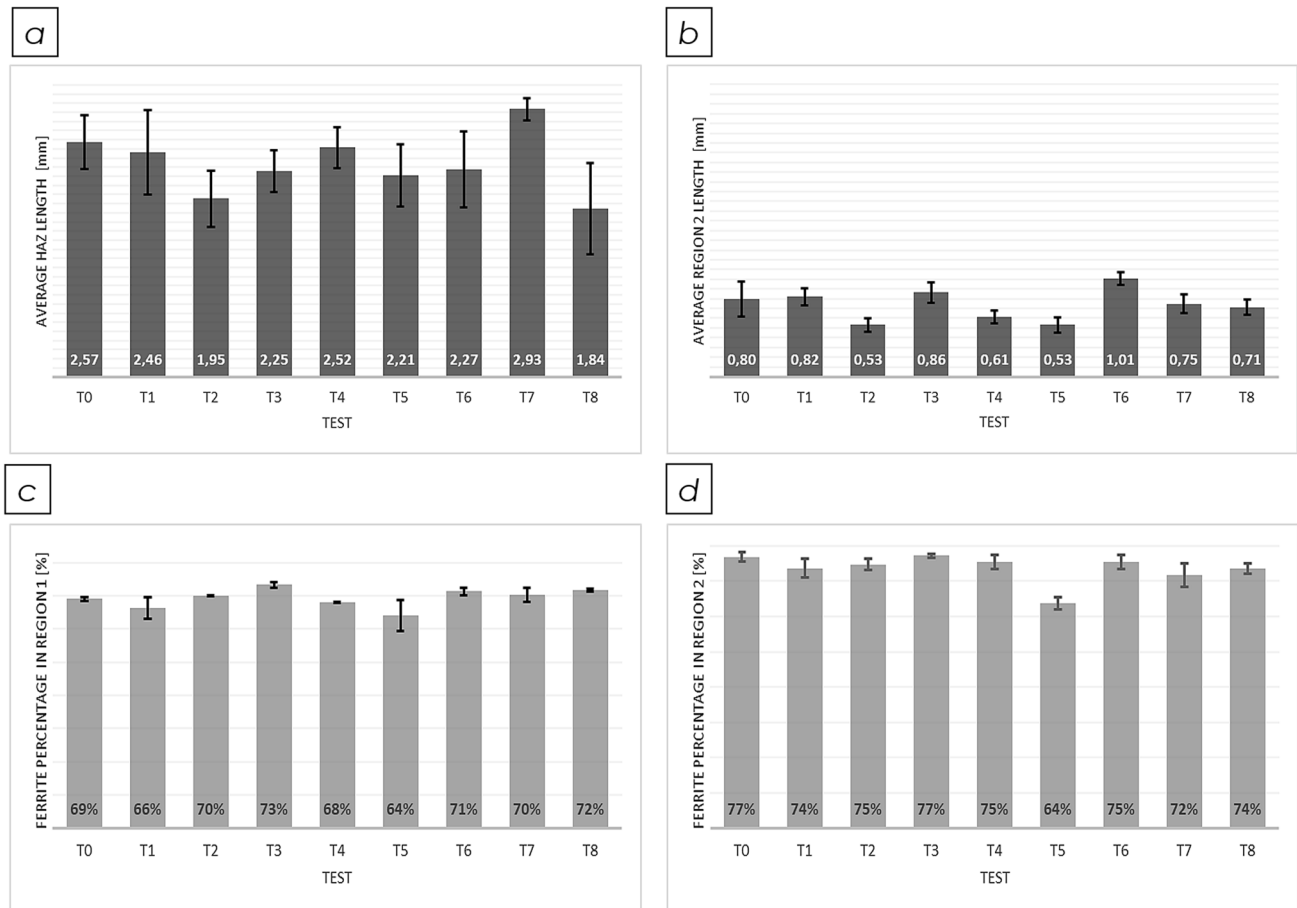


Fig. 9 **a** Average HAZ extension resulting from pass 2.1, **b** average extension of *region 2* resulting from pass 2.1, **c** ferrite content percentage in *region 1*, **d** ferrite content percentage in *region 2*

The data analysis related to *pass 2.1* revealed that both the average size of the whole HAZ (Fig. 9a) and the percentage of ferrite within both regions remained relatively consistent for all the investigated process conditions, and therefore in all the tests. In fact, the corresponding values were uniformly distributed as the process conditions changed. Specifically, the average length of the HAZ ranged from approximately 1.84 mm in test 8 to 2.93 in test 7, with an average value of 2.33 mm. Whereas the ferrite percentage in *region 1* ranged from 64% in test 5 to 73% in test 3 with an average value of 69.22%, in *region 2*, it ranged from a minimum of 64% in test 5 to a maximum of 77% in tests 0 and 3, with an average value of 73.66%.

Considering the number of tests investigated and the outcomes data distribution under different working conditions, no correlation was identified with the process parameters employed for performing the joint.

As previously mentioned, test 2, test 5 and test 7 were compared for evaluating the effect caused by *pass 2.2*. The comparison, both from a qualitative and a quantitative point of view, is reported in Fig. 10, where the macrographs and

the measurement of the average HAZ extension and the ferrite content just in *region 2*, for sake of simplicity, are depicted. The analysis revealed higher values for both the HAZ extension and ferrite percentage related to *pass 2.2* for all the tests, likely due to the different thicknesses of the welded plates. *pass 2.2*, in fact, was consistently performed on the 10-mm-thick side, resulting in a lower heat dissipation rate.

In addition to that, it is worth pointing out that the difference in the cooling rate of the welded plates, resulting from variations in plate thickness, also had an impact on the microstructure. Specifically, in *region 2*, thicker Widmanstatten ferrite was observed on the thinner plate side (10-mm thickness). For instance, in test 7, a comparison of micrographs at 50x magnification revealed the characteristic microstructure of *region 2* produced by *pass 2.2* (Fig. 11a) and *pass 2.1* (Fig. 11b).

The metallographic investigation highlighted that the percentage of ferrite in the two regions remained fairly consistent when modifying the main welding parameters while maintaining a constant specific heat input.

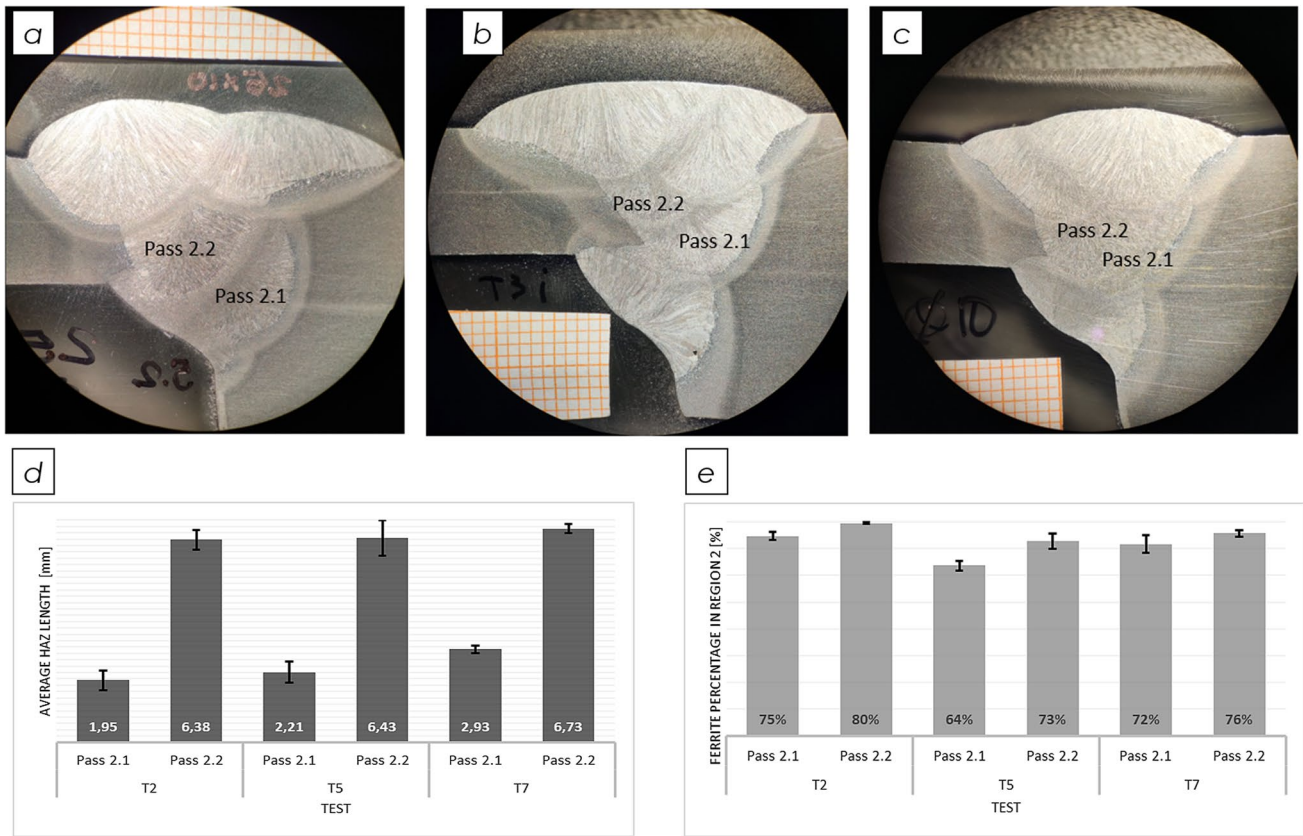
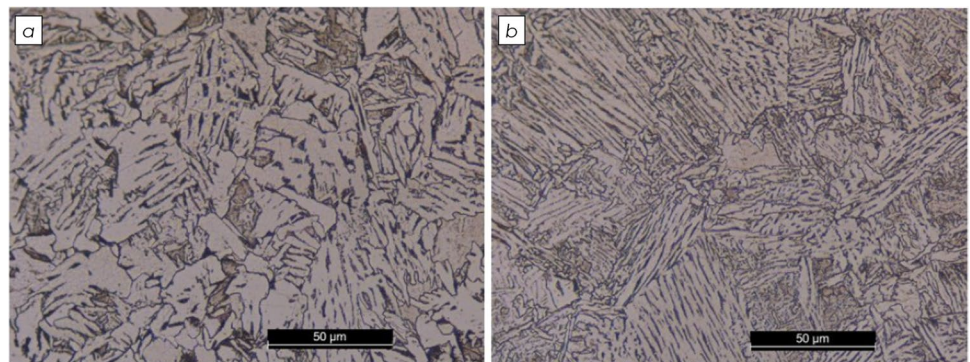


Fig. 10 Macrographs of welding test **a** T2, **b** T5, **c** T7; **d** average extension of the HAZ produced by pass 2.1 and 2.2, and **e** percentage of ferrite contained in *region 2* related to pass 2.1 and 2.2

Fig. 11 Cooling rate effect on the Widmanstatten ferrite. Test 7, **a** pass 2.2 side 10 mm and **b** pass 2.1 side 25 mm



To further verify the influence of the process variables on the mechanical properties of the final joints, numerous microhardness measurements were performed across the sample, following the procedure illustrated in paragraph 3.2. To this aim, test 0, which represents the benchmark since it satisfies the required standard for the specific application field, was compared to test 8, which was performed by setting the highest value of the welding speed, maintaining always constant the specific heat input. The hardness profile aimed at showing how the hardness varied across

the identified zones, which were the welding zone, *region 1*, *region 2* and base material, for the two above-mentioned tests. As clearly seen from the histogram displayed below (Fig. 12), in both tests, the hardness values are comparable, demonstrating that the increase in the welding speed, but guaranteeing a specific heat input, does not affect the mechanical response of the joint.

Following this observation, the efficiency increase, resulting from a higher welding speed, was quantified. More in detail, in test 0, passes 2 had a welding speed of 320 mm/min

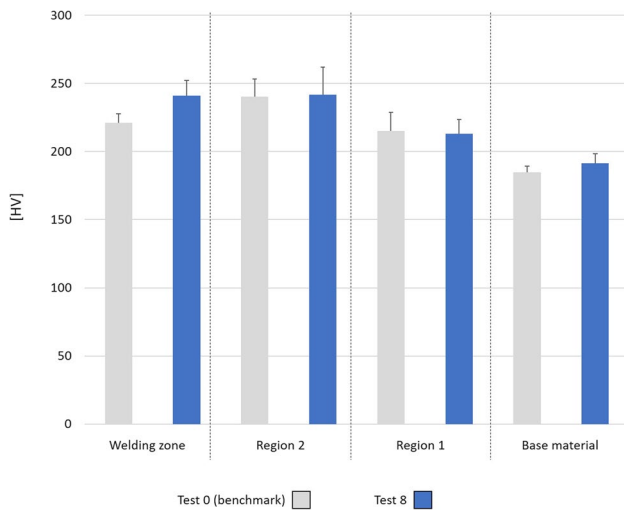


Fig. 12 Hardness profile of test 0 (benchmark) and test 8 (faster process condition)

Table 6 Comparison of T0 and T6 tests for active welding time calculation

No. of test	Pass 2 welding speed (mm/s)	Pass 3 welding speed (mm/s)	Joint length (mm)	Active welding time (s)
Test 0	5.33	9.07	400	238.24
Test 8	9.60	12.80		145.83

and passes 3 of 544 mm/min, while in test 8, passes 2 had a welding speed of 576 mm/min and passes 3 had a speed of 768 mm/min. The time necessary to perform pass 1 was not included in the calculation, as the same parameters were used for all tests, as well as the time between pass 1 and the next ones, which was also ignored since it was the same in all tests. Therefore, only the active time of the welding process was calculated by considering the four passes and the total length of the plates (400 mm). Table 6 reports the active welding times of the compared tests. Test 0 lasted approximately 4 min while test 8 approximately 2 min and half. The time saving provided by the new process conditions, which guarantee the same mechanical properties of the joint, was around 61%. This represents a significant result for such kind of industrial applications where the joints to perform are much larger than the ones herein examined; therefore, the competitive industrial advantage provided in these terms becomes significant.

5 Conclusion

This study focused on the submerged arc welding technology employed on carbon steel plates, aiming at demonstrating the process optimization based on substantial experimental

evidences. Plates of different thicknesses were joined using multi-pass welding according to an experimental plan. The joints were meticulously analysed from macroscopic and microscopic perspectives to understand the effects of the thermal cycle on the heat-affected zone. The key welding process parameters, and the resulting specific heat input, significantly impact on the microstructure of the weld bead first and, subsequently, on the heat-affected areas. The percentage of ferrite and perlite of the welded steel was measured, and the analysis of the results has shown how the process efficiency and, therefore, the productivity can be improved while ensuring the required welding quality. Test 0, in fact, represented the test that satisfies the UNI EN ISO 3834 quality standards and, therefore, it was considered as the reference point for both the microstructural analysis and the hardness measurements. All the other tests were carried out gradually increasing the welding speed, and the microstructure was analysed comparing the content of ferrite to the one obtained in test 0. Furthermore, for verifying the influence of the process parameters on the mechanical properties of the joint, microhardness was measured in different zones. It was demonstrated that for the same heat input set considering the output rating of current and voltage, the welding speed increase, within a range of preset values depending on the machine, does not affect the heat-affected zone, as well as the mechanical strength of the joint. Therefore, the productivity of the welding process under investigation may be increased, but the process parameters have to be set maintaining constant the specific heat input.

These findings can serve as a guide for future research and practical applications, ultimately leading to enhanced welding practices and the development of more robust and reliable welded joints.

Author contributions All authors contributed to the study conception and design, as well as to the sample preparation, data collection and analysis. The first draft of the manuscript was written by Francesco Raffaele Battista and Romina Conte, and all authors commented on previous versions of the manuscript. The final manuscript was read and approved by all authors.

Funding Open access funding provided by Università della Calabria within the CRUI-CARE Agreement. This work was supported by SMILE project (Strumenti e Metodi Intelligenti per la Digital Enterprise—SMILE, Fondo per la Crescita Sostenibile—Sportello “FABBRICA INTELLIGENTE” PON I&C 2014-2020, di cui al D.M. 5 marzo 2018 Capo III, Prog n. F/190084/03/X44—CUP: B21B19000530008).

Declarations

Competing interests The authors declare no competing interests.

Open Access This article is licensed under a Creative Commons Attribution 4.0 International License, which permits use, sharing, adaptation, distribution and reproduction in any medium or format, as long as you give appropriate credit to the original author(s) and the source,

provide a link to the Creative Commons licence, and indicate if changes were made. The images or other third party material in this article are included in the article's Creative Commons licence, unless indicated otherwise in a credit line to the material. If material is not included in the article's Creative Commons licence and your intended use is not permitted by statutory regulation or exceeds the permitted use, you will need to obtain permission directly from the copyright holder. To view a copy of this licence, visit <http://creativecommons.org/licenses/by/4.0/>.

References

- RanjanGiri S, Kumar Khamari B, Ranjan MB (2022) Joining of titanium and stainless steel by using different welding processes: a review. *Mater Today Proc* 66:505–8. <https://doi.org/10.1016/j.matpr.2022.05.590>
- Nandwani S, Vardhan S, Bagha AK (2020) A literature review on the exposure time of microwave based welding of different materials. *Mater Today Proc* 27:2526–8. <https://doi.org/10.1016/j.matpr.2019.10.056>
- Shen J, Taek Choi Y, Gonçalves R, Schell N, Yang J, Zeng Z et al (2024) Synergistic effects of Monel 400 filler wire in gas metal arc welding of CoCrFeMnNi high entropy alloy. *Mater Des* 242:112996. <https://doi.org/10.1016/j.matdes.2024.112996>
- Shen J, Agrawal P, Rodrigues TA, Lopes JG, Schell N, He J et al (2023) Microstructure evolution and mechanical properties in a gas tungsten arc welded Fe₄₂Mn₂₈Co₁₀Cr₁₅Si₅ metastable high entropy alloy. *Mater Sci Eng A* 867:144722. <https://doi.org/10.1016/j.msea.2023.144722>
- Radhakrishnan VM (2005) *Welding technology and design*. New Age International
- Banerjee A, Jha K, Petru M, Kumar R, Sharma S, Saini MS et al (2023) Fabrication and characterization of weld attributes in hot gas welding of alkali treated hybrid flax fiber and pine cone fibers reinforced poly-lactic acid (PLA) based biodegradable polymer composites: studies on mechanical and morphological properties. *J Mater Res Technol*. <https://doi.org/10.1016/j.jmrt.2023.09.252>
- Jiao J, Xu J, Jing C, Sheng L, Ru H, Xia H (2023) Laser welding process and strength enhancement of carbon fiber reinforced thermoplastic composites and metals dissimilar joint: a review. *Chinese J Aeronaut*. <https://doi.org/10.1016/j.cja.2023.02.025>
- Min J, Li Y, Li J, Carlson BE, Lin J (2015) Friction stir blind riveting of carbon fiber-reinforced polymer composite and aluminum alloy sheets. *Int J Adv Manuf Technol* 76:1403–10. <https://doi.org/10.1007/s00170-014-6364-8>
- Lionetto F, Mele C, Leo P, D'Ostuni S, Balle F, Maffezzoli A (2018) Ultrasonic spot welding of carbon fiber reinforced epoxy composites to aluminum: mechanical and electrochemical characterization. *Compos Part B Eng* 144:134–42. <https://doi.org/10.1016/j.compositesb.2018.02.026>
- Miranda MAS, Almaraz GMD, López JJV, Dominguez AE, Vilchez JAR, Juárez JCV (2023) Welding of two dissimilar polymers UHMWPE and PP, using friction stir welding and evaluation of mechanical properties. *Procedia Struct Integr* 47:310–24. <https://doi.org/10.1016/j.prostr.2023.07.094>
- Acherjee B (2021) State-of-art review of laser irradiation strategies applied to laser transmission welding of polymers. *Opt Laser Technol* 137:106737. <https://doi.org/10.1016/j.optlastec.2020.106737>
- Anwer G, Acherjee B (2022) Laser polymer welding process: fundamentals and advancements. *Mater Today Proc* 61:34–42. <https://doi.org/10.1016/j.matpr.2022.03.307>
- Sharma L, Chhibber R (2020) Study of weld bead chemical, microhardness & microstructural analysis using submerged arc welding fluxes for linepipe steel applications. *Ceram Int* 46:24615–23. <https://doi.org/10.1016/j.ceramint.2020.06.250>
- Sharma L, Chhibber R (2019) Design of TiO₂–SiO₂–MgO and SiO₂–MgO–Al₂O₃-based submerged arc fluxes for multipass bead on plate pipeline steel welds. *J Press Vessel Technol* 141:1–12. <https://doi.org/10.1115/1.4043375>
- Gunaraj V, Murugan N (1999) Application of response surface methodology for predicting weld bead quality in submerged arc welding of pipes. *J Mater Process Technol* 88:266–75. [https://doi.org/10.1016/S0924-0136\(98\)00405-1](https://doi.org/10.1016/S0924-0136(98)00405-1)
- Weman K (2003) *Welding processes handbook*. Woodhead Publishing Ltd. Elsevier. <https://doi.org/10.1533/9781855738539>
- Cunat P-J (2007) *The welding of stainless steels*. Materials and applications series, vol 3, 2nd edn. Euro Inox
- Lippold JC (2014) *Welding metallurgy and weldability*. John Wiley & Sons, Hoboken, NJ
- Saleem M, Lakshmanaswamy N (2022) Optimization of process parameters on weld bead characteristics of mild steel in submerged arc welding process. *Mater Today Proc* 62:1004–10. <https://doi.org/10.1016/j.matpr.2022.04.259>
- Küçüköner H, Karakoç H, Kahraman N (2020) Investigation of microstructure and mechanical properties of AISI2205/DIN-P355GH steel joint by submerged arc welding. *J Manuf Process* 59:566–86. <https://doi.org/10.1016/j.jmapro.2020.10.023>
- Renwick BG, Patchett BM (1976) Operating characteristics of the submerged arc process. *Weld J* 55:69
- Datta S, Bandyopadhyay A, Pal PK (2008) Mathematical modeling of process behavior of submerged arc welding using reclaimed slag. *J Manuf Sci Prod* 9:159–70. <https://doi.org/10.1515/IJMSP.2008.9.3-4.159>
- Prasad K, Dwivedi DK (2008) Some investigations on microstructure and mechanical properties of submerged arc welded HSLA steel joints. *Int J Adv Manuf Technol* 36:475–83. <https://doi.org/10.1007/s00170-006-0855-1>
- Rathi AK (2021) To study the effect of submerged arc welding parameters on bead geometry and hardness for mild steel (IS-2062A) using fractional factorial design. *Mater Today Proc* 34:525–30. <https://doi.org/10.1016/j.matpr.2020.03.106>
- Vishwakarma S, Dwivedi VK (2021) Optimization of process parameters of submerged arc welding by Taguchi method. *Mater Today Proc* 47:7067–72. <https://doi.org/10.1016/j.matpr.2021.06.141>
- Uptis E, Moen RA, Carpenter ML, Newell W, Grubb JF, Sutherland RC et al (2020) Part 2, section II—materials and specifications. Online companion guide to ASME boil. Press. Vessel Codes, ASME Press. <https://doi.org/10.1115/1.802183>
- Patel S, Patel P, Mehta V (2017) Experimental study of the effect of heat input on mechanical properties of TIG welded joints of SA516 grade 70 material. *Int J Res Sci Innov* IV:29–35
- Singh R (2021) *Arc welding processes handbook*. John Wiley & Sons, Scrivener Publishing

Publisher's Note Springer Nature remains neutral with regard to jurisdictional claims in published maps and institutional affiliations.